Junyu Li, Shuyun Cao, Xuemei Cheng, Franz Neubauer, Haobo Wang, and Meixia Lv, 2021, Migmatite and leucogranite in a continental-scale exhumed strike-slip shear zone: Implications for tectonic evolution and initiation of shearing: GSA Bulletin, https://doi.org/10.1130/B35988.1.

Supplemental Material

Text. Analytical Methods

Figure S1. (A, B, D) Deformed leucogranite shows ductile structures, K-feldspar porphyroclasts with core-mantle structure, fine quartz aggregate bands and fine-grained matrix. C. Deformed leucogranite, elongated quartz with irregular grain boundaries. E. Elongated K-feldspar porphyroclasts with blue luminescence and plagioclase presenting pink color. F, G. K-feldspar grains showing a subhedral shape from a post-shearing pegmatite. H. Subhedral crystal shape of K-feldspar and plagioclase in CL image.

Figure S2. Structures of zircons from foliated leucogranites and migmatite. Red circles indicate the location of the LA-ICPMS analysis. The spot numbers presented above the zircon images are the same spot number as listed in Table S2.

Table S1. Locations, rock type and mineralogy, zircon CL, Th/U, zircon U–Pb geochronology and the average Ti-in-zircon thermometer results of investigated samples.

Table S2. Zircon LA-ICP-MS U-Pb Dating results.

Table S3. Zircon LA-ICP-MS rare earth element results.

Table S4. Major element compositions of Migmatites and leucogranites.

Table S5. Trace element compositions of Migmatites and leucogranites.

Table S6. Electron microprobe analysis test data.

ANALYTICAL METHODS

Zircon U–Pb geochronology

Ten samples of granitic rocks and pegmatitic dikes from the ALS high-grade metamorphic belt were collected for zircon LA-ICP-MS U–Pb dating. All zircons were separated from whole-rock samples using conventional techniques. After crushing and sieving of the samples, heavy minerals were concentrated by panning and then by magnetic separation. Zircon grains were handpicked and then the grains were mounted in an epoxy disc. These zircons are then carefully polished until their cores were exposed. Cathodoluminescence (CL) images of zircons combined with reflected light and transmitted light images were used to morphologically distinct target areas on the zircons for LA-ICP-MS analysis. The U–Pb dating of the zircons was conducted by LA-ICP-MS at the State Key Laboratory of Geological Processes and Mineral Resources, China University of Geosciences, Wuhan. The detailed operating conditions for the laser ablation system and ICP-MS instrument and the data reduction are given in Liu et al.

(2008). A pulsed 193 nm Ar-F excimer laser at a repetition rate of 10 Hz was used for ablation. The energy density of laser ablation used in this study was 14 Jcm^{-2}. The diameter of the analyzed spot was set at 32 μm. An Agilent 7500a ICP-MS was used to measure the ion-signal intensity of the zircons. Helium was used as a carrier gas, and argon was used as the make-up gas and mixed with the carrier gas via a T-connector before entering the ICP-MS. Nitrogen was added to the central gas flow (Ar + He) of the Ar plasma to enhance the instrument sensitivity (Hu et al., 2008). Each analysis comprised a background acquisition of ca. 20–30 s (gas blank) followed by 50 s of data acquisition from the sample. Each analysis incorporated a background acquisition of ~20–30 s (gas blank) and a sample acquisition of 50 s. The Agilent Chemstation was utilized for the acquisition of each individual analysis. Off-line selection and integration of background and analyte signals, and time-drift correction and quantitative calibration for trace element analysis and U–Pb dating were performed by ICPMSDataCal (Liu et al., 2008). Time-dependent drifts of U-Th-Pb isotopic ratios were corrected using a linear interpolation (with time) for every five analyses according to the variations of standard zircon 91500 (Liu et al. 2010). Uncertainty of preferred values for the external standard 91500 was propagated to the ultimate results of the samples. All of the U–Pb ages were calculated using the Isoplot 4.15 Excel macro of Ludwig (2003).

Major and trace elemental geochemistry

Bulk-rock major and trace element compositions Whole-rock samples were crushed in a corundum jaw crusher down to 60 mesh size. Approximately 50 g was powdered in an agate ring mill to less than 200 mesh size. The major elements were analyzed using a X-ray fluorescence (Shimadzu XRF-1800) at the State Key Laboratory of Geological Processes and Mineral Resources, China University of Geosciences, Wuhan (GPMR-CUG). The analytical precision and accuracy for major elements were better than 5%. The sample preparation and analytical procedures were described in detail by Su et al. (2012). Trace elements were analyzed using an Agilent 7700x ICP-MS at GPMR. Approximately 50mg of each sample was digested in HF+HNO3 in Teflon bombs for ICP-MS analysis. The sample-digesting procedure for ICP-MS analysis and the analytical precision and accuracy for trace elements were the same as those described by Liu et al. (2008b).

EBSD and cathodoluminescence (CL) analysis

Detailed microstructural observations and electron backscatter diffraction (EBSD) measurements were conducted on thin sections from the ALS metamorphic complex. By standard, all thin sections were prepared parallel to the kinematic XZ section, i.e., parallel to the stretching lineation and, where visible, normal to the foliation. EBSD is a method that using scanning electron microscopy to obtain information on the crystallographic preferred orientation on main rock-constitutive minerals like quartz (e.g., Prior et al., 1999; Stipp et al., 2002; Liu et al., 2008; Cao et al., 2011). The experiments were carried out in State Key Laboratory of Geological Processes and Mineral Resources, China University of Geosciences (Wuhan) using a FEI Quanta 450 FEG-SEM field emission scanning electron microscope and EBSD detector to obtain and by measuring the mineral crystallographic preferred orientation (CPO). Before the experimental test, the oriented thin section has been polished precisely. Polishing was performed by using first an Al_2O_3 suspension with a particle size of 3.5 μm and 1.5 μm, respectively, to

polish the thin section, and then using a diamond suspension with a diameter of 0.5 μm and finalized using an Al_2O_3 suspension with a particle size of 0.05 μm for the final high-precision polishing. The samples were finally cleaned in an ultrasonic bath to prevent the residual of polishing fluid affecting the accuracy of the experiment. Before the test, a conductive tape attached to the thin section surface of measurement area was used to reduce charging effects as far as possible. Then the polished thin sections were put in the scanning electron microscope chamber with a 70° tilt angle, and the lineation of the thin section (structural X reference direction) is parallel to the SEM X-axis. The electron backscatter patterns (EBSP) were acquired under of low-vacuum conditions, low acceleration voltage of 20 kV, detector distance of 160 mm, the beam working distance of ca. 19–22 mm and was completed with the mode of automatic mapping. Indexing was accepted when at least six detected kikuchi bands matched with those in the standard reflector file, and the Mean Angular Deviation (MAD) is set to 1.5. After the completed test, EBSP analysis was carried out using the HKL Channel 5 software package, and the pole figure of representative lattice preferred orientation in samples was plotted in lower-hemisphere equal-area stereographic diagrams.

Cathodoluminescence (CL) is used as a powerful tool to identify mineral phases, shape and distribution. Minerals with distinct compositions show distinct colors under CL (e.g., Götze et al., 2013; Higgins, 2016; Cheng et al., 2018; Dong et al., 2019). The CL analysis was conducted by the BII CLF-2 Cathodoluminescence in the State Key Laboratory of Geological Processes and Mineral Resources, China University of Geosciences, Wuhan, China. The operating conditions were: voltage at 15 KV, current at 300 A, power at 150 W, beam current at 1 mA with a beam diameter of 30 μm, and the exposure time was 20 s.

EPMA methodology

Electron microprobe analysis (EPMA) of hornblende and plagioclase were carried out on a JEOL electron microprobe (JXA-8600) at the Department Geography and Geology, University of Salzburg, using a wavelength dispersive system. We used an acceleration voltage of 15 kV and a sample current of 40 nA. Natural and synthetic mineral standards were used to calibrate the microprobe and raw data was reduced using standard ZAF correction. The detection limits (2s) for the elements Si are Al are 0.06 wt% and 0.04 wt%, respectively, for Na, K, Mg, Mn, and Fe are 0.025 wt%.

REFERENCES CITED

Cao, S.Y., Liu, J.L., Leiss, B., Vollbrecht, A., Genser, J., Neubauer, F., and Zhao, C.Q., 2011, Initiation of left-lateral deformation along the Ailao Shan-Red River shear zone: new microstructural, textural and geochronological constraints from the Diancang Shan metamorphic massif, SW Yunnan, China: International Geology Review, v. 54, p. 348–367 https://doi.org/10.1080/00206814.2010.543789.

Cheng, X.M., Cao, S.Y., Li, J.Y., Yu, Z.P., Dong, Y.L., Lv, M.X., and Liu, J.L., 2018, Metamorphic, deformation, fluids and geological significance of low-temperature retrograde mylonites of Diancangshan metamorphic massif along Ailaoshan-Red River strike-slip fault zone: Yunnan: China: Science in China. Series D, Earth Sciences, v. 61, p. 1023–1041 https://doi.org/10.1007/s11430-017-9194-4.

Dong, Y.L., Cao, S.Y., Cheng, X.M., Liu, J.L., and Cao, H.S., 2019, Grain-size reduction of feldspar and flow of deformed granites within the Gaoligong shear zone, southwestern Yunnan: China: Science in China. Series D, Earth Sciences, v. 62, p. 1379–1398 https://doi.org/10.1007/s11430-018-9351-8.

Götze, J., Schertl, H.P., Neuser, R.D., Kempe, U., and Hanchar, J.M., 2013, Optical microscope-cathodoluminescence (OM–CL) imaging as a powerful tool to reveal internal textures of minerals: Mineralogy and Petrology, v. 107, p. 373–392 https://doi.org/10.1007/s00710-012-0256-0.

Higgins, M. D., 2016, Quantitative investigation of felsic rock textures using cathodoluminescence images and other techniques. Lithos, v. 277, p. 259-268. https://doi.org/10.1016/j.lithos.2016.05.006.

Hu, Z.C., Gao, S., Liu, Y.S., Hu, S.H., Chen, H.H., and Yuan, H.L., 2008, Signal enhancement in laser ablation ICP-MS by addition of nitrogen in the central channel gas. Journal of Analytical Atomic Spectrometry, v. 23, p. 1093–1101. http://pubs.rsc.org/doi:10.1039/B804760J.

Liu, J. L., Cao, S.Y., Zou, Y. X., Song, Z. J., 2008. EBSD analysis of rock fabrics and its application. Geological. Bulletin of China, v, 27, p. 1638-1645.

Liu, Y.S., Hu, Z.C., Gao, S., Günther, D., Xu, J., Gao, C.G., and Chen, H.H., 2008, In situ analysis of major and trace elements of anhydrous minerals by LA-ICP-MS without applying an internal standard. Chemical Geology, v. 257, p. 34–43. https://doi.org/10.1016/j.chemgeo.2008.08.004.

Liu, Y., Zong, K., Kelemen, P. B., and Gao, S., 2008b, Geochemistry and magmatic history of eclogites and ultramafic rocks from the Chinese continental scientific drill hole: subduction and ultrahigh-pressure metamorphism of lower crustal cumulates. Chemical Geology, 247, 133–153. https://doi.org/10.1016/j.chemgeo.2007.10.016.

Liu, Y.S., Gao, S., Hu, Z.C., Gao, C.G., Zong, K.Q., and Wang, D.B., 2010b, Continental and oceanic crust recycling-induced melt–peridotite interactions in the Trans-North China Orogen: U–Pb dating, Hf isotopes and trace elements in zircons of mantle xenoliths. Journal of Petrology, v. 51, p, 537–571. https://doi.org/10.1093/petrology/egp082.

Ludwig, K.R., 2003, ISOPLOT 3.00: a geochronological toolkit for microsoft excel. Berkeley Geochronology Center Special Publication, p. 1–70.

Prior, D.J., Boyle, A.P., Brenker, F.E., Cheadle, M.C., Day, A., Lopez, G., Peruzzo, L., Potts, J., Reddy, S., and Spiess, R., 1999, The application of electron backscatter diffraction and orientation contrast 788 imaging in the SEM to textural problems in rocks: The American Mineralogist, v. 84, p. 1741–1759 https://doi.org/10.2138/am-1999-11-1204.

Su, Y., Zheng, J., Griffin, W.L., Zhao, J., Tang, H., Ma, Q., and Lin, X., 2012, Geochemistry and geochronology of Carboniferous volcanic rocks in the eastern Junggar terrane, NW China: implication for a tectonic transition: Gondwana Research, v. 22, p. 1009–1029 https://doi.org/10.1016/j.gr.2012.01.004.

Stipp, M., Stünitz, H., Heilbronner, R., and Schmid, S.M., 2002, The eastern Tonale fault zone: a 'natural laboratory' for crystal plastic deformation of quartz over a temperature range from 250 to 700°C: Journal of Structural Geology, v. 24, p. 1861–1884 https://doi.org/10.1016/S0191-8141(02)00035-4.

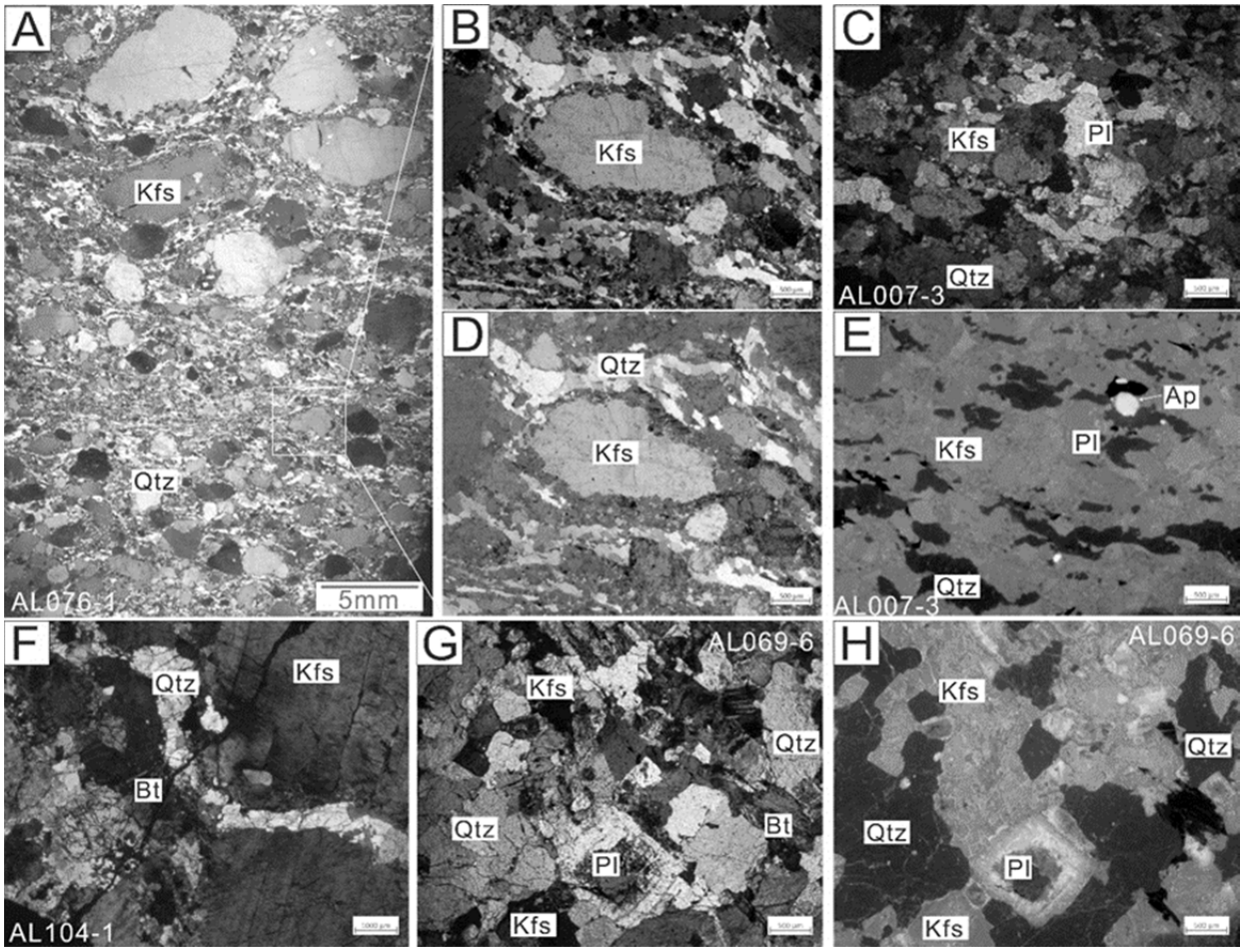

Figure S1. (A, B, D) Deformed leucogranite shows ductile structures, K-feldspar porphyroclasts with core-mantle structure, fine quartz aggregate bands and fine-grained matrix. C. Deformed leucogranite, elongated quartz with irregular grain boundaries. E. Elongated K-feldspar porphyroclasts with blue luminescence and plagioclase presenting pink color. F, G. K-feldspar grains showing a subhedral shape from a post-shearing pegmatite. H. Subhedral crystal shape of K-feldspar and plagioclase in CL image.

Figure S2. Structures of zircons from foliated leucogranites and migmatite. Red circles indicate the location of the LA-ICPMS analysis. The spot numbers presented above the zircon images are the same spot number as listed in Table S2.

Table S1 Locations, rock type and mineralogy, zircon CL, Th/U, zircon U–Pb geochronology and the average Ti-in-zircon thermometer results of investigated samples

Sample number	GPS coordinates	Rock type	Mineralogy	Zircon particle size, CL structure (L=length, w=width)	Zircon Th/U	Zircon $^{206}Pb/^{238}U$ age	Average Ti-in-zircon thermometer /℃
AL082-3	23.278443°N 102.685213°E	Migmatite/mesosome	Qtz+Kfs+Plag+Bt+Amp	L: 100–200 um, W: 40–80μm, inherited cores-rim	0.4–0.9 (core)	413-1159 Ma	862
					0.002–0.02 (rim)	34.1±0.7 Ma	724
AL082-1	23.278443°N 102.685213°E	leucogranite	Qtz+Kfs+Plag+Bt+Grt	L: 200–300 um, W: 150–200μm, inherited cores-rim	0.01–2.78 (rim)	35.1±1.0 Ma	754
AL007-3	22.975362°N 103.284926°E	leucogranitic	Qtz+Kfs+Bt+Amp	L: 60–150 um, W: 40–80μm, inherited cores-rim	0.06–0.56 (core)	281.5-732.2 Ma	816
					0.08–0.90 (rim)	31.9-39.8 Ma	781
AL076-1	23.225353°N 102.818849°E	leucogranite	Qtz+Kfs+Plag+Bt	L: 80–200 um, W: 40–100μm, inherited cores-rim and wide accretion margins	066–1.24 (core)	629.9-790.2 Ma	751
					0.001–0.007 (rim)	32.8±0.3 Ma	676
AL089-3	23.291281°N 102.597185°E	leucogranite	Qtz+Kfs+Plag+Bt+Grt	L: 150–200 um, W: 60-–100μm, distinct inherited core and very wide accretion rim	0.23–1.12 (core)	80.3±2.5 Ma 154.1±2.1Ma	810
					0.04–0.34 (rim)	34.5±1.4 Ma	736

AL089-4	23.291281°N 102.597185°E	leucogranite	Qtz+Kfs+Plag+Bt+Grt	L: 150–200 um, W: 80–100μm, distinct inherited core and very wide accretion rim	0.05–0.29 (rim)	29.7±0.4 Ma	665
AL104-1	23.372738°N, 102.372473°E	leucopegmatite	Qtz+Kfs+Plag+Mus	L: 250–300 um, W: 150–200 μm, clear oscillation zones	0.36–0.93 (rim)	25.0±0.4 Ma	749
AL069-6	23.172622°N 102.746407°E	leucogranitic	Qtz+Kfs+Plag+Bt+Grt	L: 100–150 um, W: 80–100μm, oscillation zones at the rim	0.60–1.02 (rim)	24.1±0.3 Ma	772
AL069-9	23.172622°N 102.746407°E	leucopegmatite	Qtz+Kfs+Plag+Mus	L: 120–200 um, W: 80–120μm, oscillatory zones and generally highly luminescent	0.004–0.009 (rim)	25.4±0.5 Ma	668
AL116-1	23.351811°N, 102.335140°E	leucopegmatite	Qtz+Kfs+Plag+Mus	L: 80–120 μm, W: 60-80 μm, clear oscillation zones	0.11–0.54 (rim)	23.0±0.4 Ma	721
					0.05–0.13 (core)	587.8±10.8 Ma 154.1±2.1 Ma	699